

Dynamical structural instability and its implication on the physical properties of infinite-layer nickelates

Chengliang Xia^{1,2}, Jiakuan Wu², Yue Chen¹ and Hanghui Chen^{2,3}

¹*Department of Mechanical Engineering, The University of Hong Kong, Pokfulam Road, Hong Kong SAR, China*

²*NYU-ECNU Institute of Physics, NYU Shanghai, Shanghai 200122, China*

³*Department of Physics, New York University, New York, NY 10003, USA*

Abstract

We use first-principles calculations to find that in infinite-layer nickelates $R\text{NiO}_2$, the widely studied tetragonal $P4/mmm$ structure is only dynamically stable for early lanthanide elements $R = \text{La-Sm}$. For late lanthanide elements $R = \text{Eu-Lu}$, an imaginary phonon frequency appears at $A = (\pi, \pi, \pi)$ point. For those infinite-layer nickelates, condensation of this phonon mode into the $P4/mmm$ structure leads to a more energetically favorable $I4/mcm$ structure that is characterized by an out-of-phase rotation of “ NiO_4 square”. Special attention is given to two borderline cases: PmNiO_2 and SmNiO_2 , in which both the $P4/mmm$ structure and the $I4/mcm$ structure are local minimums, and the energy difference between the two structures can be fine-tuned by epitaxial strain. Compared to the $P4/mmm$ structure, $R\text{NiO}_2$ in the $I4/mcm$ structure has a substantially reduced Ni $d_{x^2-y^2}$ bandwidth, a smaller Ni d occupancy, a “cleaner” Fermi surface with a lanthanide- d -derived electron pocket suppressed at Γ point, and a decreased critical U_{Ni} to stabilize long-range antiferromagnetic ordering. All these features imply enhanced correlation effects and favor Mott physics. Our work reveals the importance of structure-property relation in infinite-layer nickelates, in particular the spontaneous “ NiO_4 square” rotation provides a tuning knob to render $R\text{NiO}_2$ in the $I4/mcm$ structure a closer analogy to superconducting infinite-layer cuprates.

I. INTRODUCTION

The discovery of superconductivity in infinite-layer nickelates $\text{Sr}_x\text{Nd}_{1-x}\text{NiO}_2$ [1] has drawn great attention [2–9] because the parent material NdNiO_2 has similar crystal and electronic structures to those of infinite-layer cuprate CaCuO_2 [10], which exhibits high-temperature unconventional superconductivity upon doping [11, 12]. Both NdNiO_2 and CaCuO_2 crystallize in a simple tetragonal $P4/mmm$ structure in which Ni (Cu) and O atoms form a flat “ NiO_4 (CuO_4) square” [13–15]. The $P4/mmm$ crystal structure has only two degrees of freedom: lattice constants a and c . As for the non-interacting electronic structure, first-principles calculations show that CaCuO_2 has only one Cu $d_{x^2-y^2}$ -derived band that crosses the Fermi level, while NdNiO_2 has two bands crossing the Fermi level [16–20]. One is Ni $d_{x^2-y^2}$ -derived band and the other band is derived from Nd d orbitals and an interstitial s orbital [21–23]. So far, the minimum theoretical model that is adequate to describe the low-energy physics of infinite-layer NdNiO_2 has been under intensive debate and several different mechanisms for superconductivity in $\text{Sr}_x\text{Nd}_{1-x}\text{NiO}_2$ have been proposed [24–44]. Albeit there are many important differences, one thing in common is that all first-principles calculations use the $P4/mmm$ crystal structure of NdNiO_2 (either experimental one or theoretical optimized one), based on which one-particle band structure calculations (using density functional theory and its Hubbard U extension) [45–50] or more sophisticated many-body electronic structure calculations (such as dynamical mean field theory and GW) [51–63] are performed. On the experimental side, in addition to $\text{Sr}_x\text{Nd}_{1-x}\text{NiO}_2$, recently superconductivity is also observed in $\text{Sr}_x\text{Pr}_{1-x}\text{NiO}_2$ [64–66], $\text{Sr}_x\text{La}_{1-x}\text{NiO}_2$ [67] and $\text{Ca}_x\text{La}_{1-x}\text{NiO}_2$ [68, 69]. Thus it is anticipated that superconductivity should be observed in the entire lanthanide series of infinite-layer nickelates $R\text{NiO}_2$. In particular, Refs. [70, 71] perform a systematic study on the electronic structure of $R\text{NiO}_2$ in the $P4/mmm$ structure as R traverses the lanthanide series and find promising trends that favor superconductivity.

In this work, we use first-principles calculations to show that the widely studied $P4/mmm$ structure of infinite-layer nickelates is only dynamically stable for early lanthanide elements $R = \text{La-Sm}$. For late lanthanide elements $R = \text{Eu-Lu}$, an imaginary phonon mode appears at $A = (\pi, \pi, \pi)$ point in the $P4/mmm$ structure of $R\text{NiO}_2$. The imaginary phonon mode corresponds to an out-of-phase rotation of “ NiO_4 square” about the z axis. Condensation of this unstable phonon mode into the $P4/mmm$

structure leads to a more energetically favorable crystal structure with lower symmetry (space group $I4/mcm$). Attention is given to two borderline cases PmNiO_2 and SmNiO_2 , which have two local minimums: the $P4/mmm$ structure and the $I4/mcm$ structure. Epitaxial strain can be used to fine-tune the energy difference between the two crystal structures.

Compared to the $P4/mmm$ structure, infinite-layer $R\text{NiO}_2$ in the new $I4/mcm$ structure has a distinct electronic structure: the Ni $d_{x^2-y^2}$ bandwidth is substantially reduced (by about 0.5 eV) and Ni d occupancy decreases; the Fermi surface becomes “cleaner” because one lanthanide- d -derived electron pocket disappears at the Γ point; the critical U_{Ni} to stabilize a long-range antiferromagnetic ordering in $R\text{NiO}_2$ is smaller. All these features imply that with the “ NiO_4 square” rotation, correlation effects will be enhanced and Mott physics will play a more prominent role in the new $I4/mcm$ structure than in the $P4/mmm$ structure, when local interaction is added on Ni d orbitals [72]. In particular, our results suggest that among the lanthanide series of infinite-layer nickelates, SmNiO_2 is the most promising candidate to crystallize in the $I4/mcm$ structure, which renders it a closer analogy to superconducting infinite-layer cuprates.

II. COMPUTATIONAL DETAILS

We perform density functional theory (DFT) [73, 74] calculations within the *ab initio* plane-wave approach, as implemented in the Vienna Ab-initio Simulation Package (VASP) [75, 76]. We use projected augmented wave (PAW) pseudopotentials with the 4*f* electrons placed in the core (except for La), explicitly to avoid complication that arises from treating the localized 4*f* electrons. We employ generalized gradient approximation (GGA) for the exchange-correlation functional with Perdew-Burke-Ernzerhof (PBE) parametrization [77]. The theoretical lattice constants of $R\text{NiO}_2$ are in good agreement with the available experimental structure information (see Supplementary Materials [78] Sec. I) [15, 50, 79]. We use an energy cutoff of 600 eV. Charge self-consistent calculations are converged to 10^{-7} eV. Both cell and internal atomic positions are fully relaxed until each force component is smaller than 1 meV/Å and pressure on the cell is smaller than 0.1 kB. We use the finite-displacement method to calculate the full phonon dispersion with the aid of Phonopy [80]. A supercell that consists of

$3 \times 3 \times 3$ primitive cells is used to calculate the force constants and dynamical matrices. The primitive cell of the $P4/mmm$ structure has one formula of $RNiO_2$ (i.e. 4 atoms), while the primitive cell of the $I4/mcm$ structure has two formulae of $RNiO_2$ (i.e. 8 atoms) in order to accommodate the rotation of “NiO₄ square”. For the 4-atom $P4/mmm$ cell, we use a Monkhorst-Pack \mathbf{k} mesh of $14 \times 14 \times 14$ to sample the first Brillouin zone. For the 8-atom $I4/mcm$ cell, we use a Monkhorst-Pack \mathbf{k} mesh of $10 \times 10 \times 10$ to sample the first Brillouin zone. For ease of comparison, when calculating the electronic structure, Fermi surface and long-range magnetic ordering, we use the 8-atom cell for both $P4/mmm$ and $I4/mcm$ structures. This cell-doubling is also necessary to accommodate the rocksalt antiferromagnetic ordering in the $P4/mmm$ structure. To study the energy evolution as a function of “NiO₄ square” rotation, we use a linear interpolation and generate an intermediate crystal structure between the fully-relaxed $P4/mmm$ and $I4/mcm$ crystal structures. The “NiO₄ square” rotation angle continuously changes with an interpolation parameter λ (more details are found in Supplementary Materials [78] Sec. II). When we impose a bi-axial strain on infinite-layer nickelates, the out-of-plane c axis is fully relaxed in order to minimize the total energy. When calculating $Sr_xR_{1-x}NiO_2$, we use virtual crystal approximation (VCA) [81]. To break spin symmetry and study magnetic order, we use the charge-only DFT+ U + J method [82–84] (by setting LDAUTYPE = 4 in VASP). This method is such that the exchange-correlation functional only depends on charge density but not on spin density; thereby, spin symmetry is only broken by the U/J terms that are added to the Kohn-Sham potential, while the exchange splitting that arises from the spin-dependent exchange-correlation functional is disabled. By setting the parameter $U/J = 0$ in the charge-only DFT+ U + J method, the non-spin-polarized DFT results are recovered. The calculations of Ni d projected magnetic moment and Ni d occupancy use the default VASP value for the radius of sphere which is 1.11 Å. We also use the charge-only DFT+ U + J method to test phonon spectrum for a few representative $RNiO_2$ (see Supplementary Materials [78] Sec. VIII) [79, 85, 86].

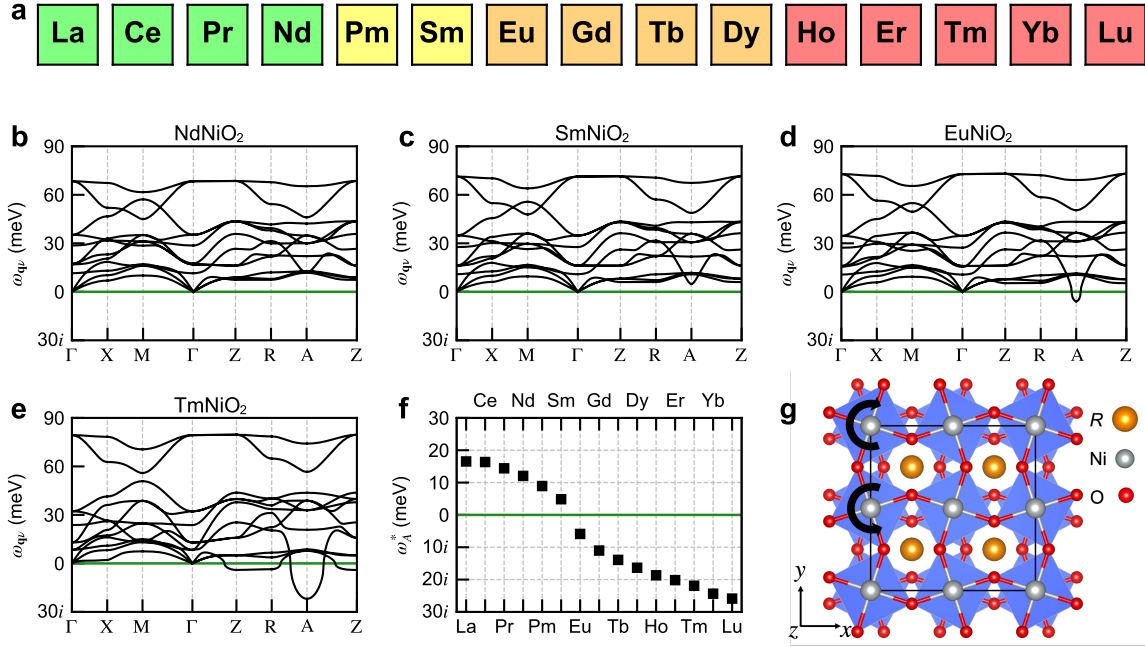


Figure 1: Phonon properties of infinite-layer $R\text{NiO}_2$ in the $P4/mmm$ structure. **a**: The series of lanthanide elements. Different colors are used to distinguish four categories of phonon dispersions, whose prototypes are shown in **b-e**. **b**: Phonon dispersion of infinite-layer NdNiO_2 in the $P4/mmm$ structure. **c**: Phonon dispersion of infinite-layer SmNiO_2 in the $P4/mmm$ structure. **d**: Phonon dispersion of infinite-layer EuNiO_2 in the $P4/mmm$ structure. **e**: Phonon dispersion of infinite-layer TmNiO_2 in the $P4/mmm$ structure. **f**: Frequency of the lowest phonon mode at $A = (\pi, \pi, \pi)$ point ω_A^* for the entire lanthanide series of infinite-layer $R\text{NiO}_2$ in the $P4/mmm$ structure. **g**: The lowest phonon mode at A point of infinite-layer $R\text{NiO}_2$ in the $P4/mmm$ structure.

III. RESULTS AND DISCUSSION

A. Phonon spectrum

We calculate the phonon dispersion of the fully-relaxed $P4/mmm$ structure for the entire lanthanide series of infinite-layer $R\text{NiO}_2$. We find that the complete set of phonon dispersions (see Supplementary Materials [78] Sec. II) can be classified into four categories, which we use colors to distinguish in panel **a**. The first category includes $R=\text{La-Nd}$ (denoted by green). NdNiO_2 is the prototype, whose full phonon dispersion is shown in panel **b**. In this category, the full phonon dispersion is free of imaginary

modes and the $P4/mmm$ crystal structure is dynamically stable. The second category includes $R=Pm, Sm$ (denoted by yellow). $SmNiO_2$ is the prototype, whose full phonon dispersion is shown in panel **c**. In this category, a soft phonon develops at $A = (\pi, \pi, \pi)$ point, implying a potentially unstable mode. The third category includes $R=Eu-Dy$ (denoted by orange). $EuNiO_2$ is the prototype, whose full phonon dispersion is shown in panel **d**. In this category, the frequency of the lowest phonon mode at A point (marked as ω_A^*) becomes imaginary and the $P4/mmm$ crystal structure is dynamically unstable. The last category includes $R=Ho-Lu$ (denoted by red). $TmNiO_2$ is the prototype, whose full phonon dispersion is shown in panel **e**. In this category, the lowest phonon modes at multiple \mathbf{q} points become imaginary in the phonon dispersion, indicating that the $P4/mmm$ crystal structure is far from stable. In panel **f**, we compare the frequency of the lowest phonon mode at A point ω_A^* for the entire lanthanide series. We find that ω_A^* monotonically decreases from La to Lu and becomes imaginary when $R=Eu$ and beyond. In panel **g**, we show the lowest phonon mode at A point of the $P4/mmm$ structure, which is an out-of-phase rotation of “NiO₄ square” about the z axis. Infinite-layer nickelates with early lanthanide elements such as $NdNiO_2$ are stable against this “NiO₄ square” rotation, and their equilibrium structure is the widely-studied $P4/mmm$ structure. However, infinite-layer nickelates with late lanthanide elements become dynamically unstable when the “NiO₄ square” rotates. Condensation of this unstable mode into the $P4/mmm$ structure will lead to a more energetically favorable crystal structure, which in turn results in a new electronic structure.

B. Rotation of “NiO₄ square” and the new $I4/mcm$ structure

When the lowest phonon frequency at the A point in the $P4/mmm$ structure of $RNiO_2$ becomes imaginary ($R = Eu-Lu$), it means that condensation of this unstable phonon mode into the $P4/mmm$ structure can decrease the total energy and will result in a new crystal structure with lower symmetry. Such a crystal structure is shown in panel **a** of Fig. 2, which has space group $I4/mcm$. The primitive cell of the $I4/mcm$ structure has 8 atoms, which has three degrees of freedom: in addition to the two lattice constants a and c , there is an angle θ that characterizes the out-of-phase rotation of “NiO₄ square” about the z axis. When $\theta = 0$, the $I4/mcm$ structure is reduced to the $P4/mmm$ structure. For ease of comparison with the $I4/mcm$ structure, we show the

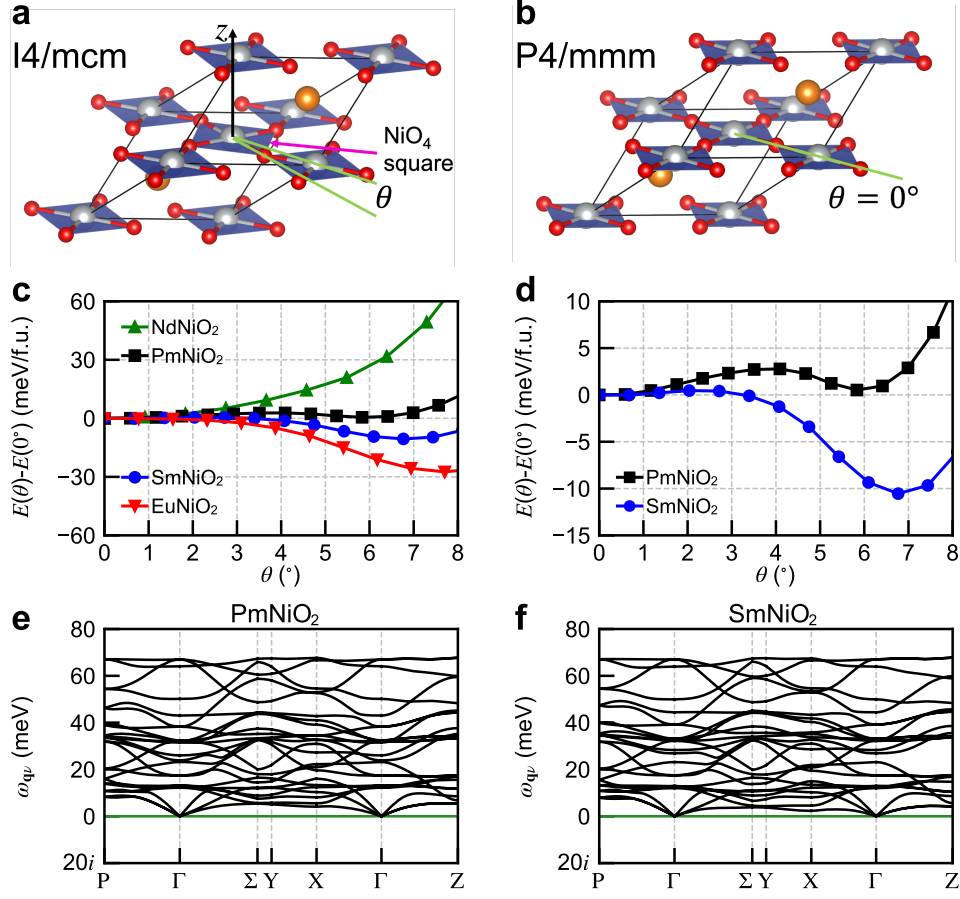


Figure 2: **a**: The primitive cell of infinite-layer nickelate $R\text{NiO}_2$ in the $I4/mcm$ structure. θ is the rotation angle of “ NiO_4 square” along the z axis. **b**: A doubled unit cell of infinite-layer nickelate $R\text{NiO}_2$ in the $P4/mmm$ structure (the $P4/mmm$ primitive cell is doubled along $[111]$ direction). $\theta = 0^\circ$ in the $P4/mmm$ structure. **c**: The energy evolution of $R\text{NiO}_2$ ($R = \text{Nd}, \text{Pm}, \text{Sm}$ and Eu) as a function of the “ NiO_4 square” rotation angle θ . The $P4/mmm$ structure is used as the energy reference. **d**: The zoom-in view of the energy evolution of PmNiO_2 and SmNiO_2 as a function of the “ NiO_4 square” rotation angle θ . **e** and **f**: The phonon dispersions of infinite-layer PmNiO_2 and SmNiO_2 in the $I4/mcm$ structure, respectively.

two-Ni unit cell of the $P4/mmm$ structure (doubling the 4-atom primitive cell along the $[111]$ direction) in panel **b**. For subsequent electronic structure, Fermi surface and long-range magnetic ordering calculations of infinite-layer $R\text{NiO}_2$, we use the 8-atom cell for both the $I4/mcm$ structure and the $P4/mmm$ structure.

To get a better understanding of the new $I4/mcm$ structure, we calculate the energy evolution of $R\text{NiO}_2$ as a function of the rotation angle θ (see panel **c** of Fig. 2, the

calculation details can be found in Supplementary Materials Sec. II [78]). We select $R = \text{Nd, Pm, Sm and Eu}$, which are near the phase boundary where the lowest phonon frequency at A point becomes imaginary. We find that the total energy of NdNiO_2 monotonically increases with the rotation angle θ , indicating that the $P4/mmm$ structure (i.e. $\theta = 0$) is stable against the rotation of “ NiO_4 square”. By contrast, the total energy of EuNiO_2 first decreases with the rotation angle θ and then increases. The energy minimum is at $\theta = 7.7^\circ$. This clearly shows that the $P4/mmm$ structure is not dynamically stable in infinite-layer EuNiO_2 . PmNiO_2 and SmNiO_2 (the second category) exhibit more interesting features in that they have two local minimums: one is at $\theta = 0$ ($P4/mmm$ structure) and the other is at $\theta > 0$ ($I4/mcm$ structure), as is shown in panel **d**. For PmNiO_2 , the energy of the $P4/mmm$ structure is slightly lower than that of the $I4/mcm$ structure by 0.5 meV/f.u. For SmNiO_2 , the energy order is reversed and the $I4/mcm$ structure becomes more stable than the $P4/mmm$ structure by 10.5 meV/f.u. Furthermore, we calculate the energy barrier from the $P4/mmm$ structure to the $I4/mcm$ structure. We find that the barrier decreases from 2.8 meV/f.u. for PmNiO_2 to 0.5 meV/f.u. for SmNiO_2 . Next we test that after condensation of the “ NiO_4 square” rotation mode, the $I4/mcm$ structure becomes dynamically stable in some infinite-layer nickelates. We perform the phonon calculation of the $I4/mcm$ structure for PmNiO_2 and SmNiO_2 . The phonon dispersions are shown in panels **e** and **f**. We find that the phonon dispersion of the $I4/mcm$ structure is free from imaginary frequencies for PmNiO_2 and SmNiO_2 . We make two comments here. First, while SmNiO_2 has two local minimums, considering the facts that 1) its $I4/mcm$ structure is energetically more favorable than the $P4/mmm$ structure, 2) the energy barrier for SmNiO_2 to transition from the $P4/mmm$ structure to the $I4/mcm$ structure is tiny (0.5 meV/f.u.), and 3) its $I4/mcm$ structure is dynamically stable, we argue that in experiments SmNiO_2 is most likely stabilized in the $I4/mcm$ structure. Second, the “ NiO_4 square” rotation is the first structural distortion that will appear in the $P4/mmm$ structure of infinite-layer nickelates $R\text{NiO}_2$ when the lanthanide element R traverses from La to Lu. For late lanthanide elements (such as Ho-Lu), more complicated structural distortions are expected to emerge in infinite-layer $R\text{NiO}_2$. The purpose of the current study is to show that just by including one more degree of freedom in the crystal structure of $R\text{NiO}_2$ (i.e. “ NiO_4 square” rotation), the resulting

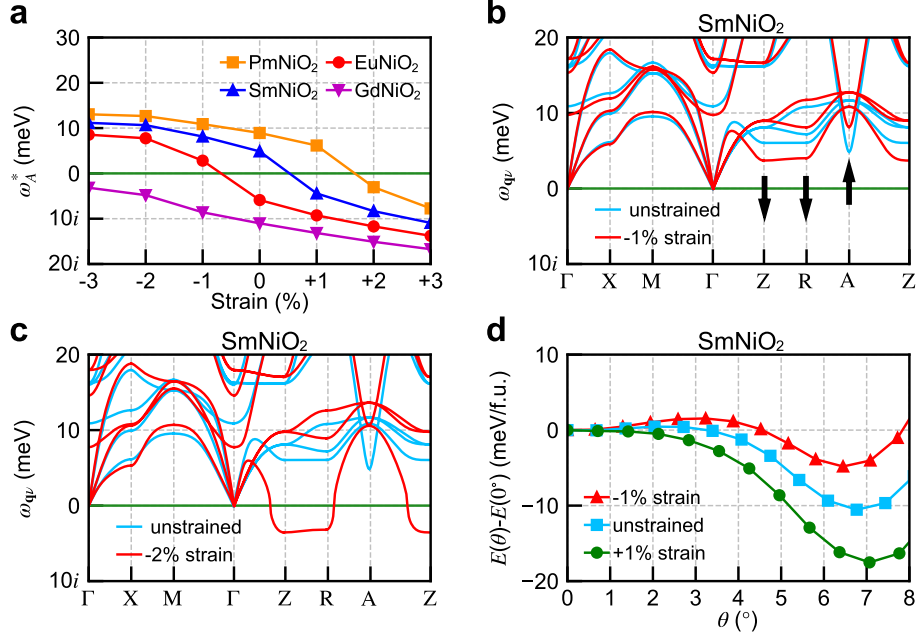


Figure 3: **a**: The lowest phonon frequency at $A = (\pi, \pi, \pi)$ point of infinite-layer $RNiO_2$ in the $P4/mmm$ structure ($R = Pm, Sm, Eu$ and Gd) as a function of biaxial strain. Negative (positive) strain means compressive (tensile) biaxial strain. **b** and **c**: The phonon dispersions of infinite-layer $SmNiO_2$ in the $P4/mmm$ structure. The cyan curves are the phonon dispersions of fully-relaxed $SmNiO_2$ (i.e. without strain). The red curves in **b** and **c** are the phonon dispersions of $SmNiO_2$ under 1% and 2% compressive strains, respectively. The black arrows highlight that with compressive strain, the lowest phonon mode at $A = (\pi, \pi, \pi)$ point is “hardened”, while the lowest phonon modes at $Z = (0, 0, \pi)$ and $R = (\pi, 0, \pi)$ are “softened”. **d**: The energy evolution of infinite-layer $SmNiO_2$ as a function of “ NiO_4 square” rotation angle θ . The red, cyan and green symbols correspond to 1% compressive strain, no strain and 1% tensile strain, respectively. For each case, the $P4/mmm$ structure is used as the energy reference.

electronic structure trends can be qualitatively different from those of the $P4/mmm$ structure (see discussion below).

C. Epitaxial strain

Before we carefully compare the physical properties of $RNiO_2$ between the $I4/mcm$ structure and the $P4/mmm$ structure, we study epitaxial strain effects first. That is

because superconductivity in infinite-layer nickelates is observed in thin films rather than in bulk [1, 3, 4, 14, 64–68, 87]. We investigate how epitaxial strain influences the phonon dispersion of infinite-layer $R\text{NiO}_2$, in particular, whether it may remove the imaginary phonon mode at A point and thus stabilize the $P4/mmm$ structure. Experimentally, oxide thin films are grown along the z axis with a biaxial strain imposed by substrates in the xy plane. The biaxial strain (either compressive or tensile) typically ranges within 3% [88].

Panel **a** of Fig. 3 shows the lowest phonon frequency at A point ω_A^* of a few infinite-layer $R\text{NiO}_2$ in the $P4/mmm$ structure as a function of biaxial strain ξ . We select $R = \text{Pm, Sm, Eu and Gd}$, which are close to the phase boundary where ω_A^* becomes imaginary (the complete phonon dispersions of those four nickelates under epitaxial strain are found in Supplementary Materials [78] Sec. III). The biaxial strain is defined as $\xi = (a_{\text{sub}} - a)/a \times 100\%$, where a_{sub} is the theoretical substrate lattice constant and a is the DFT optimized lattice constant of infinite-layer $R\text{NiO}_2$ in the $P4/mmm$ structure. For each infinite-layer $R\text{NiO}_2$, we vary the strain ξ and find that ω_A^* decreases with tensile strain and increases with compressive strain. However, we note that for infinite-layer nickelate GdNiO_2 , a compressive strain up to 3% can not remove the “ NiO_4 rotation” instability in the $P4/mmm$ structure. This is also true for other infinite-layer nickelates $R\text{NiO}_2$ with late lanthanide elements ($R = \text{Gd-Lu}$). More importantly, we find that while compressive strain helps remove the phonon instability at A point in the $P4/mmm$ structure, it may induce other phonon instabilities. Panel **b** compares the phonon dispersions of infinite-layer nickelate SmNiO_2 in the $P4/mmm$ structure under 1% compressive strain versus without epitaxial strain. It shows that compressive strain “hardens” the lowest phonon frequency at A point but “softens” the lowest phonon frequencies at Z and R points. Under a compressive strain of 2% or larger (see panel **c** and Fig. S3 in the Supplementary Materials [78]), the lowest phonon frequencies at Z and R points become imaginary in the $P4/mmm$ structure. To summarize, for infinite-layer nickelates, tensile strain increases the phonon instability at A point in the $P4/mmm$ structure; small compressive strain helps remove the phonon instability at A point but larger compressive strain can cause other phonon instabilities at Z and R points. Hence, epitaxial strain alone cannot substantially increase the stability of the $P4/mmm$ structure in infinite-layer nickelates $R\text{NiO}_2$.

On the other hand, we find that for SmNiO_2 , epitaxial strain can tune its energetics and structural properties. Panel **d** of Fig. 3 shows the energy evolution of SmNiO_2 as a function of “ NiO_4 square” rotation angle θ . We compare three different epitaxial strains: 1% compressive (-1%), no strain (0%) and 1% tensile (+1%). From 1% compressive strain to 1% tensile strain, the energy difference between the $I4/mcm$ structure and the $P4/mcm$ structure monotonically increases from 4.8 to 17.5 meV/f.u. in its magnitude (indicating that the $I4/mcm$ structure gradually becomes more stable than the $P4/mmm$ structure). At the same time, the energy barrier from the $P4/mmm$ structure to the $I4/mcm$ structure decreases from 1.5 meV/f.u. (1% compressive strain) to 0.5 meV/f.u. (no strain) and disappears (1% tensile strain). The disappearance of the energy barrier indicates that under 1% tensile strain, the $P4/mmm$ structure is no longer a local minimum in SmNiO_2 and it spontaneously transitions into the $I4/mcm$ structure. Furthermore, the equilibrium “ NiO_4 square” rotation angle θ in the $I4/mcm$ structure also increases from 6.4° to 7.1° when the epitaxial strain changes from 1% compressive to 1% tensile strain. This shows that epitaxial strain can be used as a fine-tuning knob to delicately control the structural stability of infinite-layer SmNiO_2 .

In the next three sections, we will study the entire lanthanide series of infinite-layer nickelates in the $I4/mcm$ structure and in the $P4/mcm$ structure. We compare the trends in electronic properties and magnetic properties between the two crystal structures. For demonstration, we use SmNiO_2 as a prototype.

D. $P4/mmm$ versus $I4/mcm$ structures: structural properties

Fig. 4 compares the structural properties of $R\text{NiO}_2$ between the $I4/mcm$ structure and the $P4/mmm$ structure. For infinite-layer nickelates in the first category ($R = \text{La-Nd}$), we only study the $P4/mmm$ structure because the $I4/mcm$ structure cannot be stabilized in those nickelates. Panel **a** shows the lattice constants a and c of the $I4/mcm$ and $P4/mmm$ structures. For ease of comparison to the $P4/mmm$ structure, we convert the lattice constants of the $I4/mcm$ structure into the pseudo-tetragonal lattice constants a and c (see Supplementary Materials [78] Sec. I). The general trend is similar in the two structures that a and c get smaller when R traverses the lanthanide series [71]. For a given R , the a and c lattice constants are larger in the $I4/mcm$ structure than in the $P4/mmm$ structure. Panel **b** shows the volume per Ni atom

of the $I4/mcm$ and $P4/mmm$ structures. Consistent with the trends of the lattice constants, the volume decreases as R traverses the lanthanide series. The key difference between the $I4/mcm$ structure and the $P4/mmm$ structure lies in the “NiO₄ square” rotation. In panel **c**, we show the “NiO₄ square” rotation angle θ . In the $P4/mmm$ structure, $\theta = 0$ by definition. We find that θ increases in the $I4/mcm$ structure, as we traverse from Pm to Lu. A finite θ means that the in-plane Ni-O-Ni bond angle is reduced from the ideal 180°. A direct consequence of θ is the elongation of Ni-O bond. In the $P4/mmm$ structure, the Ni-O bond length is simply half of the lattice constant a , which decreases as R traverses the lanthanide series. By contrast, in the $I4/mcm$ structure, Ni-O bond length is elongated compared to that in the $P4/mmm$ structure and it slowly increases as R traverses the lanthanide series. We note that the “NiO₄ square” rotation θ and the volume reduction are two competing forces on the Ni-O bond length. The former, which is absent in the $P4/mmm$ structure, is more dominating in the $I4/mcm$ structure. A similar picture of these two competing forces is also found in LiNbO₃ under hydrostatic pressure [89]. The different behaviors of Ni-O-Ni bond angle and Ni-O bond length in the $I4/mcm$ structure versus in the $P4/mmm$ structure will have important influences on the electronic properties of $RNiO_2$.

E. $P4/mmm$ versus $I4/mcm$ structures: electronic properties

Panel **a** of Fig. 5 compares the Ni $d_{x^2-y^2}$ bandwidth of the $I4/mcm$ structure and the $P4/mmm$ structure. Consistent with the previous studies [70, 71], the Ni $d_{x^2-y^2}$ bandwidth of the $P4/mmm$ structure monotonically increases when R traverses the lanthanide series. That is because the Ni-O bond length of the $P4/mmm$ structure monotonically decreases, which increases the Ni-O hopping and thus the bandwidth. By contrast, we find that the Ni $d_{x^2-y^2}$ bandwidth of the $I4/mcm$ structure monotonically *decreases* when R traverses the lanthanide series. That is consistent with the trend of a decreasing Ni-O-Ni bond angle and an increasing Ni-O bond length, both of which reduce the overlap between Ni- $d_{x^2-y^2}$ and O- p orbitals and thus suppress the Ni-O hopping [90]. More importantly, for a given lanthanide element R , the Ni $d_{x^2-y^2}$ bandwidth of the $I4/mcm$ structure is substantially smaller than that of the $P4/mmm$ structure. For example, for SmNiO₂, its Ni $d_{x^2-y^2}$ bandwidth is 3.2 eV in the $P4/mmm$ structure and is reduced to 2.7 eV in the $I4/mcm$ structure. This indicates that for the

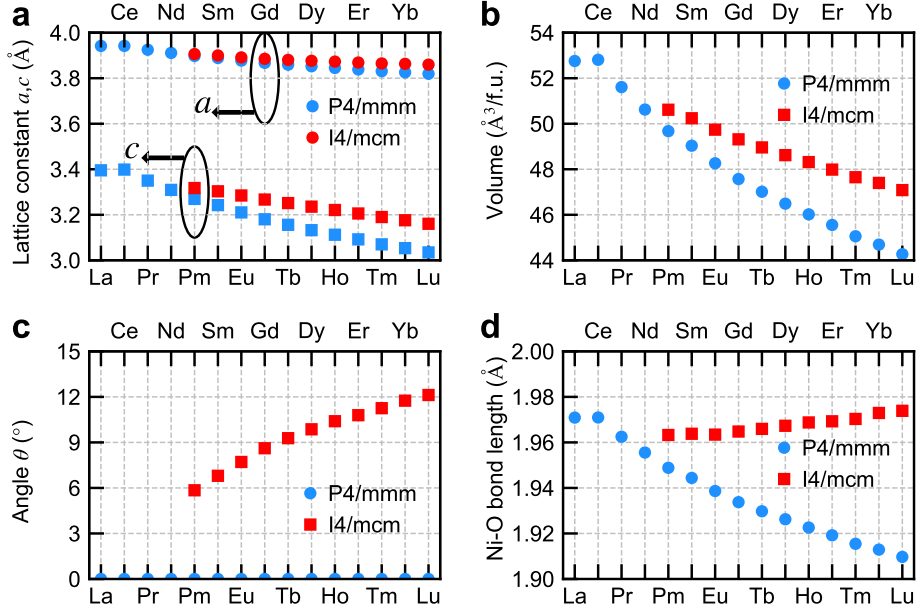


Figure 4: Crystal information of infinite-layer nickelates $R\text{NiO}_2$ in the $I4/mcm$ structure (red symbols) and in the $P4/mmm$ structure (blue symbols). **a:** The lattice constants a (circle symbols) and c (square symbols). For ease of comparison, we convert the lattice constants of the $I4/mcm$ structure into the pseudo-tetragonal lattice constants a and c . **b:** Volume per $R\text{NiO}_2$ formula (f.u.). **c:** “NiO₄ square” rotation angle θ . In the $P4/mmm$ structure, $\theta = 0^\circ$. **d:** Ni-O bond length.

same value of U on Ni $d_{x^2-y^2}$ orbital, correlation strength is increased in the $I4/mcm$ structure, compared to the $P4/mmm$ structure. In addition, we also compare the Ni d orbital occupancy N_d between the $I4/mcm$ structure and the $P4/mmm$ structure in panel **b**. Ref. [91] shows that the metal d orbital occupancy N_d is a good measure of p - d hybridization in complex oxides. We find that as R traverses the lanthanide series, $R\text{NiO}_2$ in the $P4/mmm$ structure has a progressively increased N_d . This is consistent with the previous study [71] which shows that the O- p content monotonically decreases across the lanthanide series. However, for $R\text{NiO}_2$ in the $I4/mcm$ structure, N_d almost stays a constant as R traverses the lanthanide series. By analyzing the density of states of $R\text{NiO}_2$ (see Supplementary Materials [78] Sec. VI), we find that in the $P4/mmm$ structure, running across the lanthanide series, the centroid of O- p states monotonically decreases to lower energy, by about 1 eV from La to Lu [71]. This change increases the charge-transfer energy and decreases the p - d hybridization. But in the $I4/mcm$ struc-

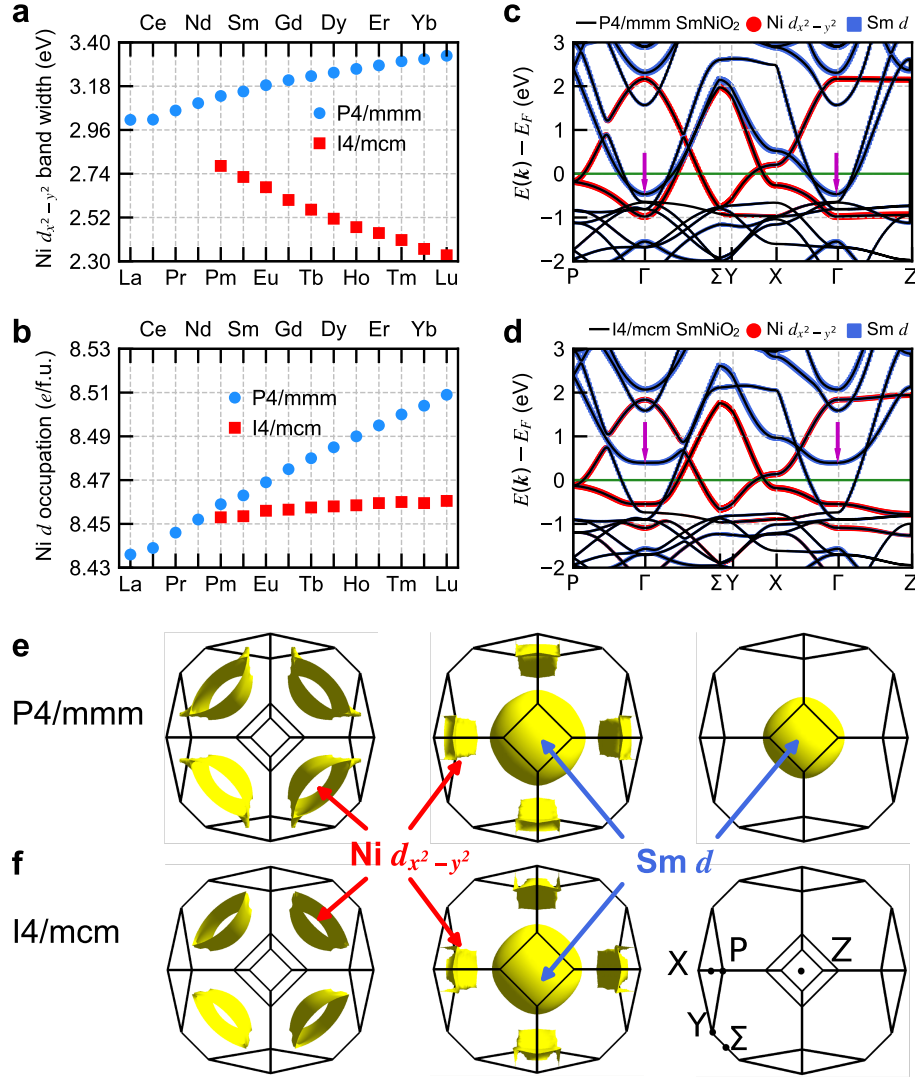


Figure 5: Electronic properties of infinite-layer nickelates $R\text{NiO}_2$ in the $I4/mcm$ structure and in the $P4/mmm$ structure. **a** and **b**: bandwidth of $\text{Ni } d_{x^2-y^2}$ orbital and $\text{Ni } d$ occupancy. The red (blue) symbols refer to the $I4/mcm$ structure (the $P4/mmm$ structure). **c** and **d**: Electronic structure of SmNiO_2 in the $P4/mmm$ structure and in the $I4/mcm$ structure, respectively. The red (blue) symbols highlight the atomic projection onto the $\text{Ni } d_{x^2-y^2}$ orbital ($\text{Sm } d$ orbitals). The purple arrows in **c** and **d** highlight that a $\text{Sm}-d$ -derived band is removed from the Fermi level and is pushed up to higher energy via the “ NiO_4 square” rotation in the $I4/mcm$ structure. **e** and **f**: Fermi surface of SmNiO_2 in the $P4/mmm$ structure and in the $I4/mcm$ structure, respectively. The red (blue) arrows highlight the Fermi surface sheets that are composed of $\text{Ni } d_{x^2-y^2}$ orbital ($\text{Sm } d$ orbitals).

ture, the “NiO₄ square” rotation counteracts this effect and the centroid of O-*p* states almost does not move across the lanthanide series. As a result, the Ni *d* occupancy N_d and *p-d* hybridization change marginally across the lanthanide series of $R\text{NiO}_2$. We note that for a given lanthanide element R , N_d is smaller in the $I4/mcm$ structure than in the $P4/mmm$ structure. A smaller N_d corresponds to a smaller critical U value for the metal-insulator transition [91], i.e. $R\text{NiO}_2$ in the $I4/mcm$ structure is closer to the Mott insulating phase than that in the $P4/mmm$ structure.

Next we study the electronic band structure and Fermi surface of SmNiO_2 as a prototype (very similar results are also obtained in infinite-layer nickelates close to the phase boundary $R\text{NiO}_2$ with $R = \text{Pm}$, Eu and Gd , see Supplementary Materials [78] Sec. V). Panel **c** of Fig. 5 shows the band structure of SmNiO_2 in the $P4/mmm$ structure. Due to the cell-doubling, there are four bands that cross the Fermi level: two are Ni- $d_{x^2-y^2}$ -derived bands and the other two are Sm-*d*-derived bands. In the unfolded Brillouin zone (BZ), the Sm-*d*-derived band crosses the Fermi level and results in two electron pockets: one is at Γ point and the other is at A point. After band folding, in the body-centered-tetragonal Brillouin zone (BCT-BZ) [71], the electron pocket that is originally at A point in the unfolded BZ is mapped to Γ point, leading to two electron pockets at Γ point. This is clearly seen in panel **e**, which shows the Fermi surface of SmNiO_2 in the $P4/mmm$ structure. These Γ -centered electron pockets are one of the main differences between infinite-layer nickelates and superconducting cuprates and their role is still under debate [16–23]. Panel **d** of Fig. 5 shows the band structure of SmNiO_2 in the $I4/mcm$ structure. Compared to the $P4/mmm$ structure, the “NiO₄ square” rotation removes one Sm-*d*-derived band (highlighted by the purple arrows) away from the Fermi surface and pushes it to higher energy. In the corresponding Fermi surface (panel **f**), one Γ -centered electron pocket vanishes. This is an interesting result in that 1) compared to the $P4/mmm$ structure, the Fermi surface of SmNiO_2 in the $I4/mcm$ structure more closely resembles that of CaCuO_2 ; and 2) the “NiO₄ square” rotation in the $I4/mcm$ structure effectively acts as hole doping in SmNiO_2 . To demonstrate the second point more clearly, we calculate the band structure and Fermi surface of $\text{Sr}_{0.2}\text{Sm}_{0.8}\text{NiO}_2$ in the $P4/mmm$ structure (see the Supplementary Materials [78] Sec. VII) and we find that they are similar to pristine SmNiO_2 in the $I4/mcm$ structure.

F. $P4/mmm$ versus $I4/mcm$ structures: magnetic properties

Next we study the magnetic properties of $R\text{NiO}_2$ and compare the $I4/mcm$ structure and the $P4/mmm$ structure. We use the charge-only DFT+ U + J method [82–84] in which the spin polarization is broken by the U/J extension rather than the spin-dependent exchange-correlation functional. The advantage of using this method is that when U/J parameters approach zero, we will recover our non-spin-polarized DFT results. We first fix the optimized crystal structure that is obtained from the non-spin-polarized (nsp) DFT calculations, upon which the electronic structure calculations are performed. This is the convention of some previous DFT+ U and DFT+dynamical mean field theory (DFT+DMFT) studies [46–48, 54–59, 71]. Then we relax the crystal structure within the charge-only DF+ U + J method and discuss the relaxation effects on magnetic properties.

We first study rocksalt antiferromagnetic ordering (ordering wave vector $\mathbf{q} = (\pi, \pi, \pi)$) in SmNiO_2 [47]. Panel **a** of Fig. 6 shows the magnetic moment on Ni atom as a function of U_{Ni} (throughout the calculations, we set $J_{\text{Ni}} = 0.15U_{\text{Ni}}$ [92]). We compare the Ni magnetic moment between the $I4/mcm$ structure and the $P4/mmm$ structure. We find that within the charge-only DFT+ U + J method, the critical effective U_{Ni} for rocksalt antiferromagnetic ordering is reduced from 1.8 eV in the $P4/mmm$ structure to 1.5 eV in the $I4/mcm$ structure. This is consistent with the bandwidth reduction effect that correlation strength is increased on Ni $d_{x^2-y^2}$ orbital in the $I4/mcm$ structure, which favors the formation of long-range magnetic ordering. Next in panel **b**, we study the entire lanthanide series of infinite-layer nickelates $R\text{NiO}_2$ and compare the critical U_{Ni} for the $I4/mcm$ structure and for the $P4/mmm$ structure. We find that the critical U_{Ni} for the $I4/mcm$ structure is always smaller than that for the $P4/mmm$ structure, and from PmNiO_2 to LuNiO_2 , the reduction in the critical U_{Ni} becomes more substantial. This feature is consistent with the trend of Ni $d_{x^2-y^2}$ bandwidth reduction (see Fig. 5a). In addition, we study the energy difference between rocksalt antiferromagnetic ordering and ferromagnetic ordering $\Delta E = E_{\text{AFM}} - E_{\text{FM}}$ as a function of U_{Ni} . Panel **c** shows that for SmNiO_2 , both in the $I4/mcm$ structure and in the $P4/mmm$ structure, when U_{Ni} exceeds the critical value (highlighted by the two dashed lines), rocksalt antiferromagnetic ordering has lower energy than ferromagnetic ordering (ΔE is negative). However, the magnitude of $|\Delta E|$ is larger in the $I4/mcm$ structure than in

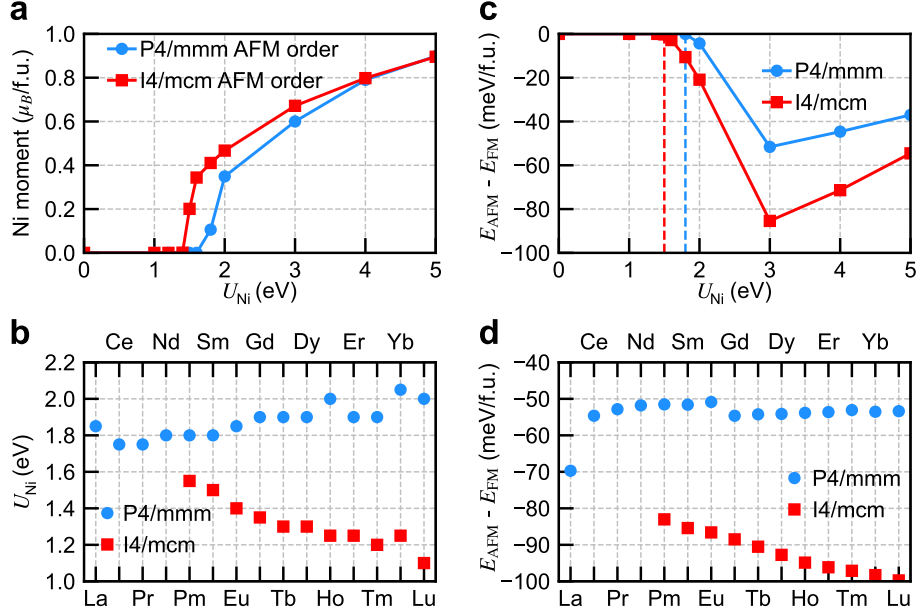


Figure 6: Magnetic properties of infinite-layer nickelates $R\text{NiO}_2$ in the $I4/mcm$ structure (red symbols) and in the $P4/mmm$ structure (blue symbols). **a**: The magnetic moment on Ni atom of SmNiO_2 in rocksalt antiferromagnetic ordering (AFM) as a function of U_{Ni} . **b**: The critical U_{Ni} for rocksalt antiferromagnetic ordering across the lanthanide series of infinite-layer nickelates $R\text{NiO}_2$. **c**: The energy difference between rocksalt antiferromagnetic ordering and ferromagnetic ordering of SmNiO_2 as a function of U_{Ni} . The dashed lines highlight the critical U_{Ni} for rocksalt antiferromagnetic ordering. **d**: The energy difference between rocksalt antiferromagnetic ordering and ferromagnetic ordering at $U_{\text{Ni}} = 3$ eV across the lanthanide series of infinite-layer nickelates $R\text{NiO}_2$.

the $P4/mmm$ structure when the long-range magnetic order is stabilized in SmNiO_2 . The results in panel **c** indicate that given the same value of U_{Ni} , the “ NiO_4 square” rotation in the $I4/mcm$ structure further stabilizes the rocksalt antiferromagnetic ordering over the ferromagnetic ordering. We repeat the same calculations for the entire lanthanide series of infinite-layer nickelates $R\text{NiO}_2$ and show in panel **d** the energy difference ΔE at $U_{\text{Ni}} = 3$ eV. We find that ΔE is negative and its magnitude is larger in the $I4/mcm$ structure than in the $P4/mmm$ structure for the entire series of $R\text{NiO}_2$ ($R = \text{Pm-Lu}$).

Next within the charge-only DFT+ U + J method, we relax the crystal structure of SmNiO_2 for each given U and J (see Supplementary Materials [78] Sec. VIII). We

find that adding U and J terms does not considerably change the optimized lattice constants and the “NiO₄ square” rotation angle. However, it is noted that a weak “cusp” feature emerges at the critical U_{Ni} when the long-range magnetic ordering is stabilized. Using the optimized crystal structure from the charge-only DFT+ U + J method, we still find that 1) the critical U_{Ni} for the $I4/mcm$ structure is smaller than that for the $P4/mmm$ structure, 2) rocksalt-antiferromagnetic ordering is more stable than ferromagnetic ordering in both crystal structures, and 3) the magnitude of the energy difference between rocksalt-antiferromagnetic ordering and ferromagnetic ordering $|\Delta E|$ is larger in the $I4/mcm$ structure than in the $P4/mmm$ structure. All these results are qualitatively consistent with the previous ones that are obtained by using the nsp-DFT optimized crystal structure.

IV. CONCLUSION

In conclusion, we perform first-principles calculations to study structural, electronic and magnetic properties of the entire lanthanide series of infinite-layer nickelates $R\text{NiO}_2$. We find that the widely-studied $P4/mmm$ structure is only dynamically stable when R is an early lanthanide element (La-Sm). For late lanthanide elements (Eu-Lu), an unstable phonon mode appears at A point in the $P4/mmm$ structure, which corresponds to an out-of-phase “NiO₄ square” rotation about the z axis. For infinite-layer nickelates with late lanthanide elements, condensation of this phonon mode in the $P4/mmm$ structure lowers the total energy and leads to a new $I4/mcm$ crystal structure. Special attention is paid to two borderline cases PmNiO_2 and SmNiO_2 , in which both the $P4/mmm$ structure and the $I4/mcm$ structure are local minimums. When epitaxial strain is imposed on infinite-layer nickelates, tensile strain further increases the dynamical instability at A point in the $P4/mmm$ structure, while compressive strain “hardens” the phonon at A point but “softens” the phonons at Z and R points in the $P4/mmm$ structure. Furthermore, epitaxial strain can fine-tune the energy difference between the $I4/mcm$ structure and the $P4/mmm$ structure when they are both dynamically stable in $R\text{NiO}_2$ (such as SmNiO_2).

We use the new $I4/mcm$ crystal structure to study the trends of electronic and magnetic properties of $R\text{NiO}_2$. We find that compared to the $P4/mmm$ structure, the Ni $d_{x^2-y^2}$ bandwidth of $R\text{NiO}_2$ is substantially reduced in the $I4/mcm$ structure,

which implies an increased correlation strength in the new $I4/mcm$ structure. In addition, the Ni d occupancy of $RNiO_2$ gets smaller in the $I4/mcm$ structure than that in the $P4/mmm$ structure, which means a small critical U_{Ni} for the metal-insulator transition [91]. Furthermore, the electronic structure and Fermi surface of $RNiO_2$ become “cleaner” in the $I4/mcm$ structure than in the $P4/mmm$ structure, because one lanthanide- d -derived band is removed from the Fermi level and thus a lanthanide- d -derived electron pocket disappears at Γ point. Finally, the critical U_{Ni} to stabilize the rocksalt antiferromagnetic ordering in $RNiO_2$ is reduced from the $P4/mmm$ structure to the $I4/mcm$ structure. All these results imply that correlation effects are enhanced and Mott physics plays a more important role in the new $I4/mcm$ crystal structure of infinite-layer $RNiO_2$. Hence, if $RNiO_2$ in the $I4/mcm$ crystal structure can be synthesized in experiment, it will provide a closer analogy to infinite-layer cuprate $CaCuO_2$. Our work suggests that among the lanthanide series of infinite-layer nickelates, the most promising candidate to crystallize in the $I4/mcm$ structure is $SmNiO_2$.

We finally note that structure-property relations have been widely studied in complex oxides, such as perovskite nickelates and manganites [93–97]. Spontaneous structural distortions, such as Jahn-Teller, breathing, rotations and tilts of oxygen octahedra, turn out to have substantial impacts on the physical properties of complex oxides [98–102]. Our work reveals a similar coupling between crystal structure and electronic structure in infinite-layer nickelates $RNiO_2$: by substituting the lanthanide element R , we can control the rotation of “ NiO_4 square”, which tunes the underlying electronic structure and may potentially favor superconductivity.

Note added: after the completion of our work, we became aware of Refs. [103–105], which also study structural distortions in infinite-layer nickelates $RNiO_2$ and $YNiO_2$. The authors of Ref. [103] find that $YNiO_2$ is also prone to the “ NiO_4 square” rotation. The authors of Ref. [104] show that due to the R -to-Ni cation mismatch, the “ NiO_4 square” is prone to various types of rotations. For R of a small ionic radius such as Y, the ground state structure has the orthorhombic $Pbnm$ symmetry with the $a^-a^-c^+$ rotation pattern. For R of a moderate ionic radius such as Gd, the ground state structure has the tetragonal $I4/mcm$ symmetry with the $a^0a^0c^-$ rotation, which is consistent with our results. The authors of Ref. [105] also find the dynamical instability of “ NiO_4 square” rotation in infinite-layer nickelates $RNiO_2$. In addition, they study the electronic and

magnetic properties of $R\text{NiO}_2$ at finite temperatures.

Acknowledgement

We are grateful to Andrew Millis for useful discussions.

-
- [1] D. Li, K. Lee, B. Y. Wang, M. Osada, S. Crossley, H. R. Lee, Y. Cui, Y. Hikita, and H. Y. Hwang, *Nature* **572**, 624 (2019).
- [2] M. Hepting, D. Li, C. J. Jia, H. Lu, E. Paris, Y. Tseng, X. Feng, M. Osada, E. Been, Y. Hikita, et al., *Nature Materials* **19**, 381 (2020).
- [3] S. Zeng, C. S. Tang, X. Yin, C. Li, M. Li, Z. Huang, J. Hu, W. Liu, G. J. Omar, H. Jani, et al., *Physical Review Letters* **125**, 147003 (2020).
- [4] D. Li, B. Y. Wang, K. Lee, S. P. Harvey, M. Osada, B. H. Goodge, L. F. Kourkoutis, and H. Y. Hwang, *Physical Review Letters* **125**, 027001 (2020).
- [5] Q. Gu, Y. Li, S. Wan, H. Li, W. Guo, H. Yang, Q. Li, X. Zhu, X. Pan, Y. Nie, et al., *Nature Communications* **11**, 6027 (2020).
- [6] B. H. Goodge, D. Li, K. Lee, M. Osada, B. Y. Wang, G. A. Sawatzky, H. Y. Hwang, and L. F. Kourkoutis, *Proceedings of the National Academy of Sciences of the United States of America* **118**, e2007683118 (2021).
- [7] B. Y. Wang, D. Li, B. H. Goodge, K. Lee, M. Osada, S. P. Harvey, L. F. Kourkoutis, M. R. Beasley, and H. Y. Hwang, *Nature Physics* **17**, 473 (2021).
- [8] D. Zhao, Y. B. Zhou, Y. Fu, L. Wang, X. F. Zhou, H. Cheng, J. Li, D. W. Song, S. J. Li, B. L. Kang, et al., *Physical Review Letters* **126**, 197001 (2021).
- [9] H. Lu, M. Rossi, A. Nag, M. Osada, D. F. Li, K. Lee, B. Y. Wang, S. Agrestini, Z. X. Shen, E. M. Been, et al., *Science* **373**, 213 (2021).
- [10] G. A. Sawatzky, *Nature* **572**, 592 (2019).
- [11] M. G. Smith, A. Manthiram, J. Zhou, J. B. Goodenough, and J. T. Markert, *Nature* **351**, 549 (1991).
- [12] M. Azuma, Z. Hiroi, M. Takano, Y. Bando, and Y. Takeda, *Nature* **356**, 775 (1992).
- [13] T. Siegrist, S. M. Zahurak, D. W. Murphy, and R. S. Roth, *Nature* **334**, 231 (1988).
- [14] Q. Li, C. He, J. Si, X. Zhu, Y. Zhang, and H.-H. Wen, *Communications Materials* **1**, 16 (2020).
- [15] B. X. Wang, H. Zheng, E. Krivyakina, O. Chmaissem, P. P. Lopes, J. W. Lynn, L. C. Gallington, Y. Ren, S. Rosenkranz, J. F. Mitchell, et al., *Physical Review Materials* **4**, 084409 (2020).

- [16] P. Jiang, L. Si, Z. Liao, and Z. Zhong, *Physical Review B* **100**, 201106 (2019).
- [17] A. S. Botana and M. R. Norman, *Physical Review X* **10**, 011024 (2020).
- [18] J. Karp, A. S. Botana, M. R. Norman, H. Park, M. Zingl, and A. Millis, *Physical Review X* **10**, 021061 (2020).
- [19] P. Adhikary, S. Bandyopadhyay, T. Das, I. Dasgupta, and T. Saha-Dasgupta, *Physical Review B* **102**, 100501 (2020).
- [20] H. Zhang, L. Jin, S. Wang, B. Xi, X. Shi, F. Ye, and J.-W. Mei, *Physical Review Research* **2**, 013214 (2020).
- [21] Y. Nomura, M. Hirayama, T. Tadano, Y. Yoshimoto, K. Nakamura, and R. Arita, *Physical Review B* **100**, 205138 (2019).
- [22] Y. Gu, S. Zhu, X. Wang, J. Hu, and H. Chen, *Communications Physics* **3**, 84 (2020).
- [23] M. Hirayama, T. Tadano, Y. Nomura, and R. Arita, *Physical Review B* **101**, 075107 (2020).
- [24] L.-H. Hu and C. Wu, *Physical Review Research* **1**, 032046 (2019).
- [25] Y. Wang, C. J. Kang, H. Miao, and G. Kotliar, *Physical Review B* **102**, 161118 (2020).
- [26] M. Jiang, M. Berciu, and G. A. Sawatzky, *Physical Review Letters* **124**, 207004 (2020).
- [27] L. Si, W. Xiao, J. Kaufmann, J. M. Tomczak, Y. Lu, Z. Zhong, and K. Held, *Physical Review Letters* **124**, 166402 (2020).
- [28] B. Geisler and R. Pentcheva, *Physical Review B* **102**, 020502 (2020).
- [29] H. Sakakibara, H. Usui, K. Suzuki, T. Kotani, H. Aoki, and K. Kuroki, *Physical Review Letters* **125**, 077003 (2020).
- [30] R. He, P. Jiang, Y. Lu, Y. Song, M. Chen, M. Jin, L. Shui, and Z. Zhong, *Physical Review B* **102**, 035118 (2020).
- [31] X. Wu, D. Di Sante, T. Schwemmer, W. Hanke, H. Y. Hwang, S. Raghu, and R. Thomale, *Physical Review B* **101**, 060504 (2020).
- [32] P. Werner and S. Hoshino, *Physical Review B* **101**, 041104 (2020).
- [33] G. M. Zhang, Y. F. Yang, and F. C. Zhang, *Physical Review B* **101**, 020501 (2020).
- [34] Z. Wang, G. M. Zhang, Y. F. Yang, and F. C. Zhang, *Physical Review B* **102**, 220501 (2020).
- [35] Y.-H. Zhang and A. Vishwanath, *Physical Review Research* **2**, 023112 (2020).
- [36] F. Bernardini, V. Olevano, and A. Cano, *Physical Review Research* **2**, 013219 (2020).

- [37] F. Bernardini and A. Cano, *Journal of Physics : Materials* **3**, 03LT01 (2020).
- [38] Z. Liu, C. Xu, C. Cao, W. Zhu, Z. F. Wang, and J. Yang, *Physical Review B* **103**, 045103 (2021).
- [39] X. Wan, V. Ivanov, G. Resta, I. Leonov, and S. Y. Savrasov, *Physical Review B* **103**, 075123 (2021).
- [40] T. Plienbumrung, M. Daghofer, and A. M. Oleś, *Physical Review B* **103**, 104513 (2021).
- [41] O. I. Malyi, J. Varignon, and A. Zunger, arxiv (2021), 2107.01790, URL <http://arxiv.org/abs/2107.01790>.
- [42] C. Peng, H.-C. Jiang, B. Moritz, T. P. Devereaux, and C. Jia, arxiv (2021), 2110.07593, URL <http://arxiv.org/abs/2110.07593>.
- [43] P. Choubey and I. M. Eremin, *Physical Review B* **104**, 144504 (2021).
- [44] C. J. Kang and G. Kotliar, *Physical Review Letters* **126**, 127401 (2021).
- [45] J. Krishna, H. Labollita, A. O. Fumega, V. Pardo, and A. S. Botana, *Physical Review B* **102**, 224506 (2020).
- [46] M. Y. Choi, K. W. Lee, and W. E. Pickett, *Physical Review B* **101**, 020503 (2020).
- [47] Z. Liu, Z. Ren, W. Zhu, Z. Wang, and J. Yang, *npj Quantum Materials* **5**, 31 (2020).
- [48] M.-Y. Choi, W. E. Pickett, and K.-W. Lee, *Physical Review Research* **2**, 033445 (2020).
- [49] Y. Zhang, L. F. Lin, W. Hu, A. Moreo, S. Dong, and E. Dagotto, *Physical Review B* **102**, 195117 (2020).
- [50] R. Zhang, C. Lane, B. Singh, J. Nokelainen, B. Barbiellini, R. S. Markiewicz, A. Bansil, and J. Sun, *Communications Physics* **4**, 118 (2021).
- [51] V. M. Katukuri, N. A. Bogdanov, O. Weser, J. Van Den Brink, and A. Alavi, *Physical Review B* **102**, 241112 (2020).
- [52] V. Olevano, F. Bernardini, X. Blase, and A. Cano, *Physical Review B* **101**, 161102 (2020).
- [53] J. Karp, A. Hampel, M. Zingl, A. S. Botana, H. Park, M. R. Norman, and A. J. Millis, *Physical Review B* **102**, 245130 (2020).
- [54] S. Ryee, H. Yoon, T. J. Kim, M. Y. Jeong, and M. J. Han, *Physical Review B* **101**, 064513 (2020).
- [55] F. Lechermann, *Physical Review B* **101**, 081110 (2020).
- [56] F. Lechermann, *Physical Review X* **10**, 041002 (2020).

- [57] I. Leonov, S. L. Skornyakov, and S. Y. Savrasov, *Physical Review B* **101**, 241108 (2020).
- [58] F. Petocchi, V. Christiansson, F. Nilsson, F. Aryasetiawan, and P. Werner, *Physical Review X* **10**, 041047 (2020).
- [59] F. Lechermann, *Physical Review Materials* **5**, 044803 (2021).
- [60] M. Kitatani, L. Si, O. Janson, R. Arita, Z. Zhong, and K. Held, *npj Quantum Materials* **5**, 59 (2020).
- [61] J. Karp, A. Hampel, and A. J. Millis, *Physical Review B* **103**, 195101 (2021).
- [62] I. Leonov, *Journal of Alloys and Compounds* **883**, 160888 (2021).
- [63] A. L. Kutepov, *Physical Review B* **104**, 085109 (2021).
- [64] M. Osada, B. Y. Wang, B. H. Goodge, K. Lee, H. Yoon, K. Sakuma, D. Li, M. Miura, L. F. Kourkoutis, H. Y. Hwang, et al., *Nano Letters* **20**, 5735 (2020).
- [65] M. Osada, B. Y. Wang, K. Lee, D. Li, and H. Y. Hwang, *Physical Review Materials* **4**, 121801 (2020).
- [66] X. Ren, Q. Gao, Y. Zhao, H. Luo, X. Zhou, and Z. Zhu, *arxiv* (2021), 2109.05761, URL <http://arxiv.org/abs/2109.05761>.
- [67] M. Osada, B. Y. Wang, B. H. Goodge, S. P. Harvey, K. Lee, D. Li, L. F. Kourkoutis, and H. Y. Hwang, *Advanced Materials* p. 2104083 (2021).
- [68] S. W. Zeng, C. J. Li, L. E. Chow, Y. Cao, Z. T. Zhang, C. S. Tang, X. M. Yin, Z. S. Lim, J. X. Hu, P. Yang, et al., *arxiv* (2021), 2105.13492, URL <http://arxiv.org/abs/2105.13492>.
- [69] P. Puphal, Y.-M. Wu, K. Fürsich, H. Lee, M. Pakdaman, J. A. N. Bruin, J. Nuss, Y. E. Suyolcu, P. A. van Aken, B. Keimer, et al., *arxiv* (2021), 2106.13171, URL <http://arxiv.org/abs/2106.13171>.
- [70] J. Kapeghian and A. S. Botana, *Physical Review B* **102**, 205130 (2020).
- [71] E. Been, W. S. Lee, H. Y. Hwang, Y. Cui, J. Zaanen, T. Devereaux, B. Moritz, and C. Jia, *Physical Review X* **11**, 011050 (2021).
- [72] P. A. Lee, N. Nagaosa, and X. G. Wen, *Reviews of Modern Physics* **78**, 17 (2006).
- [73] P. Hohenberg and W. Kohn, *Physical Review* **136**, B864 (1964).
- [74] W. Kohn and L. J. Sham, *Physical Review* **140**, A1133 (1965).
- [75] M. C. Payne, M. P. Teter, D. C. Allan, T. A. Arias, and J. D. Joannopoulos, *Reviews of Modern Physics* **64**, 1045 (1992).

- [76] G. Kresse and J. Furthmuller, *Physical Review B* **54**, 11169 (1996).
- [77] J. P. Perdew, K. Burke, and M. Ernzerhof, *Physical Review Letters* **77**, 3865 (1996).
- [78] See Supplementary Material at [URL] for more details.
- [79] H. Lin, D. J. Gawryluk, Y. M. Klein, S. Huangfu, E. Pomjakushina, F. von Rohr, and A. Schilling, arxiv (2021), 2104.14324, URL <http://arxiv.org/abs/2104.14324>.
- [80] A. Togo and I. Tanaka, *Scripta Materialia* **108**, 1 (2015).
- [81] L. Bellaiche and D. Vanderbilt, *Physical Review B* **61**, 7877 (2000).
- [82] H. Park, A. J. Millis, and C. A. Marianetti, *Physical Review B* **92**, 035146 (2015).
- [83] J. Chen, A. J. Millis, and C. A. Marianetti, *Physical Review B* **91**, 241111 (2015).
- [84] H. Chen and A. J. Millis, *Physical Review B* **93**, 045133 (2016).
- [85] M. A. Hayward, M. A. Green, M. J. Rosseinsky, and J. Sloan, *Journal of the American Chemical Society* **121**, 8843 (1999).
- [86] M. A. Hayward and M. J. Rosseinsky, *Solid State Sciences* **5**, 839 (2003).
- [87] C. He, X. Ming, Q. Li, X. Zhu, J. Si, and H.-H. Wen, *Journal of Physics: Condensed Matter* **33**, 265701 (2021).
- [88] D. G. Schlom, L. Q. Chen, X. Pan, A. Schmehl, and M. A. Zurbuchen, *Journal of the American Ceramic Society* **91**, 2429 (2008).
- [89] C. Xia, Y. Chen, and H. Chen, *Journal of Physics: Condensed Matter* **34**, 025501 (2021).
- [90] D. P. Kumah, A. S. Disa, J. H. Ngai, H. Chen, A. Malashevich, J. W. Reiner, S. Ismail-Beigi, F. J. Walker, and C. H. Ahn, *Advanced Materials* **26**, 1935 (2014).
- [91] X. Wang, M. J. Han, L. De'Medici, H. Park, C. A. Marianetti, and A. J. Millis, *Physical Review B* **86**, 195136 (2012).
- [92] G. Giovannetti and M. Capone, *Physical Review B* **90**, 195113 (2014).
- [93] M. L. Medarde, *Journal of Physics Condensed Matter* **9**, 1679 (1997).
- [94] M. B. Salamon and M. Jaime, *Reviews of Modern Physics* **73**, 583 (2001).
- [95] G. Catalan, *Phase Transitions* **81**, 729 (2008).
- [96] S. Middey, J. Chakhalian, P. Mahadevan, J. W. Freeland, A. J. Millis, and D. D. Sarma, *Annual Review of Materials Research* **46**, 305 (2016).
- [97] S. Catalano, M. Gibert, J. Fowlie, J. Íñiguez, J.-M. Triscone, and J. Kreisel, *Reports on Progress in Physics* **81**, 046501 (2018).

- [98] J. M. Rondinelli and C. J. Fennie, *Advanced Materials* **24**, 1961 (2012).
- [99] N. A. Benedek and C. J. Fennie, *Journal of Physical Chemistry C* **117**, 13339 (2013).
- [100] X. Zhai, L. Cheng, Y. Liu, C. M. Schlepütz, S. Dong, H. Li, X. Zhang, S. Chu, L. Zheng, J. Zhang, et al., *Nature Communications* **5**, 4283 (2014).
- [101] Z. Liao, M. Huijben, Z. Zhong, N. Gauquelin, S. Macke, R. J. Green, S. Van Aert, J. Verbeeck, G. Van Tendeloo, K. Held, et al., *Nature Materials* **15**, 425 (2016).
- [102] P. Chen, M. N. Grisolia, H. J. Zhao, O. E. González-Vázquez, L. Bellaiche, M. Bibes, B. G. Liu, and J. Íñiguez, *Physical Review B* **97**, 024113 (2018).
- [103] F. Bernardini, A. Bosin, and A. Cano, arxiv (2021), 2110.13580, URL <http://arxiv.org/abs/2110.13580>.
- [104] Á. A. C. Álvarez, S. Petit, L. Iglesias, W. Prellier, M. Bibes, and J. Varignon, arxiv (2021), 2112.02642, URL <https://arxiv.org/abs/2112.02642v1>.
- [105] Y. Zhang, J. Zhang, X. He, J. Wang, and P. Ghosez, arxiv (2022), 2201.00709, URL <https://arxiv.org/pdf/2201.00709.pdf>.